Nanoscience and Nanotechnology 2024, 13(1): 1-9
DOI: 10.5923/j.nn.20241301.01

Effects of Different Zn Doping Concentration on the Optical and Structural Properties of TiO_2 Nanoparticles

Gakuru Simon Waweru, Sharon Kiprotich*, Peter Waithaka

Department of Physical and Biological Sciences, Murang'a University of Technology, Murang'a, Kenya

Abstract Zn-doped TiO_2 nanoparticles (Z-T NPs) were successfully synthesized using the sol-gel method. Titanium isopropoxide, ethanol, and diethanolamine were used in the ratio of 1:6:1 as the metal precursor, solvent precursor, and refluxing agent, respectively. The Z-T NPs were characterized using Fourier Transform Infrared (FTIR), X-ray Diffraction (XRD), Scanning Electron Microscope (SEM), and UV-Vis reflectance spectroscopy. FTIR analysis showed vibrations in the fingerprint region at wave number 668 cm^{-1}, which were attributed to the Zn-O stretching vibration, and at wave number 1033 cm^{-1} for Ti-O-Zn asymmetrical stretching vibration. XRD analysis of the 0% Z-T NPs showed the formation of the anatase phase with the plane (200) as the preferred orientation. An increase of Zn % mol caused planes (105) and (211) to convolve. Debye-Scherer equation showed crystallite size decreased when the Zn dopants were introduced; 10% had the smallest crystallite size and 5% had the largest crystallite size. The crystallite size was inversely proportional to Specific Surface Area, Dislocation density, and Full Width at Half Maximum. SEM images indicated improved crystal structure with increased sintering, aggregation, and agglomeration. EDS endorsed the doping process by having Zn atoms in the doped Z-T NPs. The optical analysis showed an increase in band gap energy from 4.43 to 5.14 eV for 0% and 3% Z–T NPs, respectively.

Keywords Z-T NPs, Doping, Crystallite size, Band gap, Sol-gel method

1. Introduction

The Dye-sensitized solar cell (DSSC) TiO_2-based photoanode is a promising 3rd generation photovoltaic cell. They are in the limelight for a prospective greener energy source due to their low cost and simple manufacturing method, flexibility, environmentally friendly and comparatively high efficiency of 12.3% [1-5]; other converters of light include hybrid perovskite [6], p-n junction [7], and silicon-based solar cells [8]. Recently, studies have been oriented toward enhancing greener energy conversion by improving DSSCs' main components: the nanocrystal photoanode, dye, counter cathode electrode, and electrolyte [9]. However, the efficiency solely lies in the capacity of the photoactive nanocrystal electrode to harvest light and transport photoelectrons that are injected from the photo-excited dye of the semiconductor at the conduction band [10].

Titanium dioxide (TiO_2) is a polymorph with the rutile, anatase, and brookite phases [11]. When used as a photoanode, the anatase is more efficient than rutile phase in triggering reactions under solar illumination [12]. However, its relatively high band gap of 3.2 eV falls in the Ultra Violet region of the solar spectrum and in the abundantly visible spectrum, TiO_2 is transparent and has a high electron/ hole (e^-/h^+) recombination rate; electrons recombine with holes when they encounter each in the presence of suitable electron acceptor or recombination centers, releasing energy in the form of light or heat hindering its commercial use [11].

Studies to improve the efficiency and performance of TiO_2 as a semiconductor, have been to lower its band gap. It can be achieved through doping with foreign atoms. Doping has been found to modify the crystal structure, conductivity, band position, and change surface state by introducing intermediate energy levels that enhance electron transition with low excitation energy [13]; they include Al^{3+}, Cu^{2+}, Mn^{2+}, $Fe^{3+,}$ and Zn^{2+}.Zn can easily fit into the crystal structure of Ti due to its similar ionic radius of 0.74 Å to 0.75 Å for Zn^{2+} and Ti^{4+}, respectively [14]. Incorporation of Zn^{2+} into the TiO_2 host will lead to a significant increase in photoelectric properties since the number of valence electrons of Zn^{2+} is lower than Ti^{4+}; the excess of the hole can create an acceptor band near that of the TiO_2 [15].

Jin, E M. *et al*. [16] reported a longer recombination time of 2.338×10^{-2} s and a shorter electron transport time of 3.423×10^{-2} s were observed for 3 mmol Zn doped TiO_2. Meesombad K *et al.* [17] reported a single phase of Zn-doped TiO_2 was present at doping amounts of 2.5, 5, and 10% and 2.5 mol % Zn was the potential candidate for glutamate-sensing application. Dubey, R S. *et al.* [18] reported a 34% conversion efficiency of DSSC for Zn-doped TiO_2 samples. Rajaramanan

* Corresponding author:
Skiprotich@mut.ac.ke (Sharon Kiprotich)
Received: Apr. 15, 2024; Accepted: May 3, 2024; Published: May 13, 2024
Published online at http://journal.sapub.org/nn

T *et al.* [19] reported a significant enhancement in power conversion efficiency was observed with 1.0 mol % Zn-doped TiO_2-based DSSC with 35% efficiency greater than the control. Sharafi M *et al.* [20] reported that the efficiency of Perovskite solar cells increased by doping 2 mol % Zinc to the mesoporoustitania electron transport layer from 9.74% to 13.76%.

TiO_2 doped with Zn^{2+} ions has led to improved electron transfer, improving the efficiency of DSSC; however, a comprehensive study of the optimum amount and effect of high doping levels of Zn on TiO_2 has not yet been thoroughly investigated and reported. Investigating the effects of (1, 2, 3, 5, 7, 9, and 10%) Zn-doped TiO_2 will significantly improve the existing applications and form a basis for unlocking other possible applications. Sol-gel was preferred due to its excellent output of compounds with similar molecular structures, relatively cheap, its easiness of operation; one may use different solvents or metal precursors, and, more importantly, crystal or powder formed is pure, fine, and of uniform size [21].

2. Methodology

2.1. Materials

The following materials were used in the synthesis process: tetra isopropoxide (TTIP, > 99.90%), absolute ethanol (> 99.90%), and diethanolamine (> 99.3%), all purchased from Sigma-Adrich. Ammonium hydroxide, Hydrochloric acid, and Zinc (ii) nitrate (> 96%) were purchased from A.B.Chem. Co., Ltd. All reagents were used as supplied by the manufacturer.

2.2. Synthesis of Z-T and T NPs

A 30 mL mixture of TTIP and ethanol in a 1:6 volume ratio was added in a 50 mL glass beaker placed on a magnetic stirrer at room temperature and stirred for 30 min. With a pH meter, its pH was dropped to 7 using a stock solution of HCl or NH_4OH and stirred for 10 min. Various dopant amounts of Zinc Nitrate ($Zn(NO_3)_3$) were added separately to the sol and stirred for 15 min. After that, they were transferred to a hot magnetic stirrer at 78℃, and 6 mL of diethanolamine added dropwise and stirred for 30 min where a gel would have formed. A white precipitate would appear after stirring for the first 5 min and when placed in a hot magnetic plate, it dissolved. The gel was left to age for at least 12 h before annealing in a muffle furnace for 2h. The un-doped T NPs were synthesized using the above procedure without adding the dopant ($Zn(NO_3)_3$). The aged gel was annealed in a muffle furnace at 500℃ for 2h to give uniform nanoparticles of TiO_2 in the anatase phase.

2.3. Characterization of the Samples

Fourier Transform Infrared spectrophotometer IR Spirit Shimadzu model was used to analyze the chemical composition by showing the functional group vibrations of the synthesized Z-T NPs. X-ray diffraction (XRD) data were collected using ARL EQUINOX 100 at 40 V, 0.9 mA, CuKα radiation (**λ**= 1.5406 Å) and a scanning range of 20°-100° to obtain the crystal structure and the phase of the synthesized % mol Z-T NPs. Surface morphology and composition of the Z-T NPs were analyzed using the Phenom XL G2 Scanning Electron Microscope. A double-beam UV-Vis 1800 Shimadzu model was used to analyze optical properties at a wavelength ranging from 200 nm to 1100 nm at a fast scanning speed; the Tauc equation was employed in the optical analysis.

3. Results and Discussion

3.1. FTIR Analysis

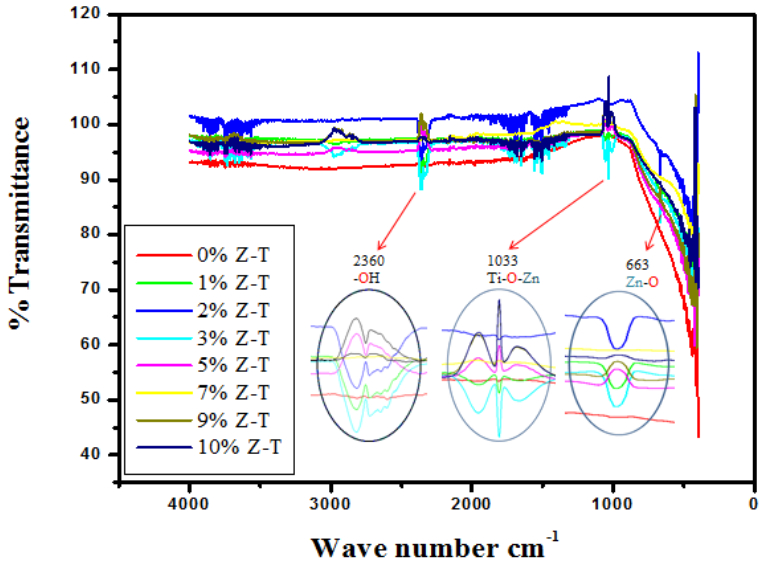

Figure 1. FTIR spectra on the effect of different Zn-doped concentrations on the functional groups of TiO_2 NPs

The presence of intra-molecular and inter–molecular interactions, molecular geometry, and functional groups present in Z-T NPs was provided by a Fourier Transform Infrared Spectroscopy (FTIR). FTIR has two types of vibration: stretching and bending vibration. Stretching vibration is classified into symmetrical and anti-symmetrical and occurs when the interatomic distance continuously changes along the bond axis bond between two atoms. The vibration is called bending vibration when there is a change in the angle between two bonds. Bending vibrations occur in the same plane for which we can have wagging, scissoring, twisting, or rocking vibrations [22]. **Figure 1** shows the FTIR spectra of the different % Z-T NPs annealed at 500℃, showing main bands at fingerprint region (< 1500 cm^{-1}) that are 668 cm^{-1} and 1033 cm^{-1} and functional group region (> 1500 cm^{-1}) at wave number 2360 cm^{-1}. The symmetric stretching and scissoring bending vibration at wave number 668 cm^{-1} is assigned to the Zn-O stretching mode. This vibration is absent at 0% but present at 1% Z-T NPs. It confirms that Zn atoms introduced new intermolecular interactions and functional groups that can be detected at that wave number. When T NPs were annealed at different temperature, the vibration was assigned to Ti-O-Ti. It was absent at temperature below 500℃ and present at and above 600℃, where its vibration intensity increased as the annealing temperature was increased [23]. The anti-symmetric stretching vibration and a twist bending at wave number 1033 cm^{-1} are assigned to the Ti-O-Zn stretching mode. In our study on the effects of growth temperature on TiO_2 NPs, the vibration at wave number 1033 cm^{-1} was assigned to Ti-O-Ti: a symmetric stretching and scissoring bending vibration [23]. It confirms that the Zn atoms are incorporated and fill in the positions of Ti atoms in the crystal and do not form a new separate compound. The difference in the two stretching vibration modes, that is, symmetric for un-doped and anti-symmetric for doped, is associated with introducing different bonding angles from the different ionic bonds of the dopant and host, making it have a twist bending vibration. The anti-symmetrical vibrations caused a wagging bending vibration that occurred at 5% doping and above as characterized by the different orientation for 1, 2, and 3% Z- T NPs to that of 5, 7, 9, and 10% Z-T NPs; the difference is of 180° to each other. It emanated from the rotation of the Zn and Ti atoms and different weight distribution in the lattice, which caused a twisting and rocking motion of atoms in the crystal. The stretching at wavenumber 2360 cm^{-1} is assigned to –OH from the solvent precursor ethanol and the refluxing agent diethanolamine forming Ti-OH.

3.2. XRD analysis

Figure 2 shows the XRD diffraction patterns of different % Z-T NPs samples annealed at 500℃. The 2 θ (37.9, 48.0, 53.8, 54.8, 62.0, 68.8, 70.0, and 75.0) correspond to the reflection from 004, 200, 105, 211, 204, 116,220, 215 crystal planes of the tetragonal titanium dioxides structure. All diffraction peaks agreed with reported JCPDS card no 84-1286 for anatase. Planes (105) and (211) are found to convolve and form one peak at 10 mol % doping. The two planes are close to each other therefore, when Zn atoms cause broadening of peaks, they convolve. The Z-T NPs preferred plane (200). It doesn't change its position and intensity.

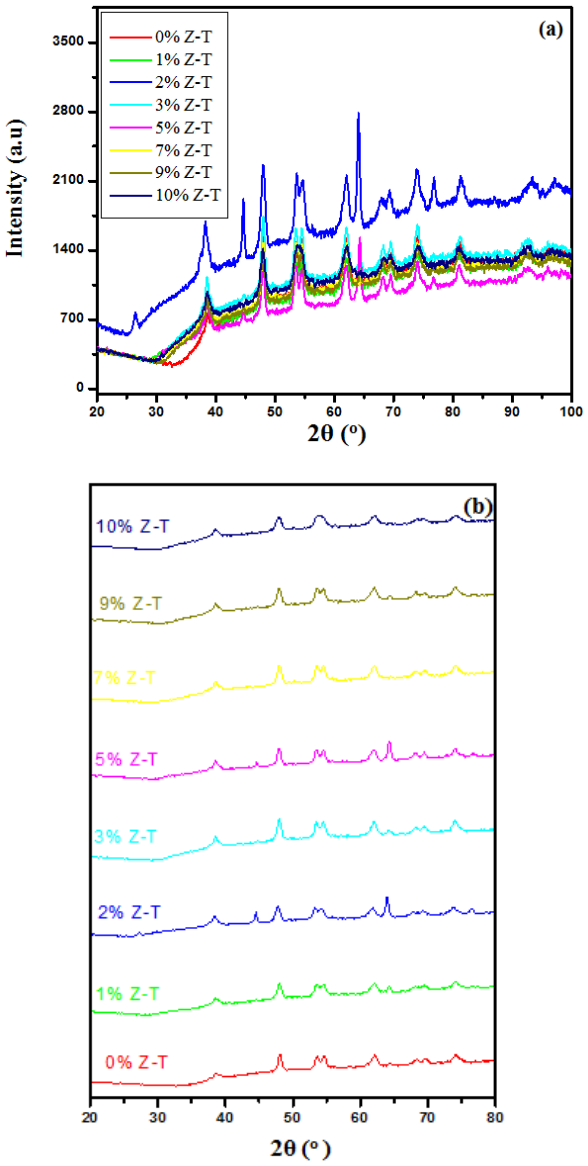

Figure 2. X-ray diffraction patterns for **(a)** merge overlaid and **(b)** stacked graphs for different % Z-T NPs annealed at 500℃

The lattice parameters a and c for the tetragonal structure were calculated using the following **Eq (1)**

$$\frac{1}{(d_{hkl})^2} = \frac{h^2+k^2}{a^2} + \frac{l^2}{c^2} \quad (1)$$

Where h, k, and l are the miller indices of the peak and d_{hkl} is the inter-planar spacing obtained from Bragg's law **Eq (2)** [24] for planes (200) and (204).

$$d_{hkl} = \frac{n\lambda}{2\,Sin\,(\theta)} \quad (2)$$

λ is the wavelength of the incident X-ray (1.5406 Å), n is the diffraction order (1), and θ is the peak position in radians.

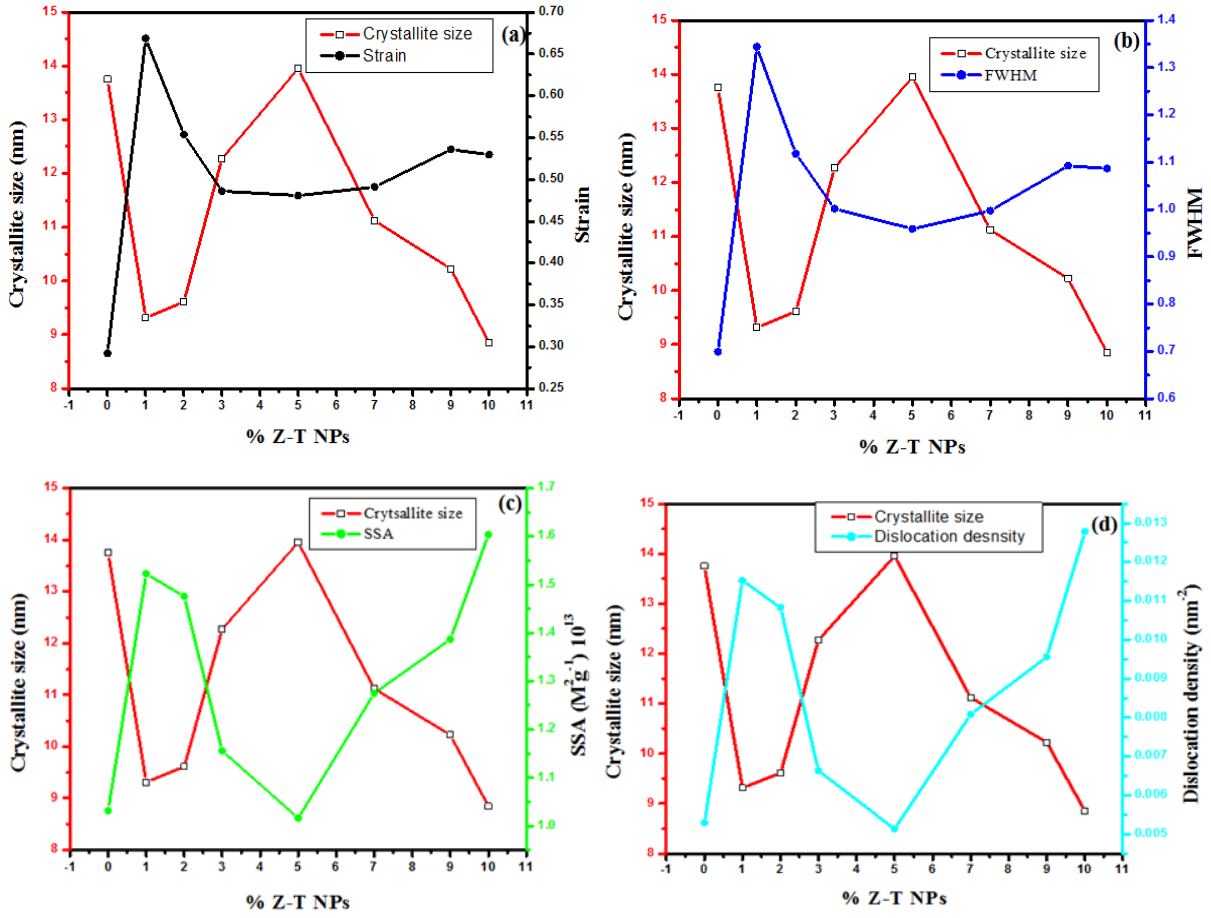

Figure 3. Plot displaying comparison on the **(a)** Strain, **(b)** FWHM, **(c)** SSA, and **(d)** dislocation density with crystallite size of different % Z-T NPs

Table 1. Calculated average values of Crystallite size, FWHM, Strain, SSA, and Dislocation density for different % Z-T NPs calculated from XRD pattern

% Z-T NPs	Crystallite size (nm)	FWHM (^{o})	Strain (ε), lines/ nm^2	Specific surface area, $M^2g^{-1} \times 10^{13}$	Dislocation density(δ), lines/ nm^3
0 % Z-T NPs	13.75	0.69918	0.29208	1.03159	0.00529
1 % Z-T NPs	9.32	1.34392	0.66852	1.52271	0.01152
2 % Z-T NPs	9.61	1.11803	0.55360	1.47584	0.01083
3 % Z-T NPs	12.28	1.00193	0.48614	1.15534	0.00663
5 % Z-T NPs	13.95	0.95881	0.48060	1.01645	0.00514
7 % Z-T NPs	11.13	0.99737	0.49086	1.27523	0.00808
9 % Z-T NPs	10.23	1.09268	0.53594	1.38701	0.00956
10 % Z-T NPs	8.85	1.08677	0.52952	1.60367	0.01278

Abbreviation: FWHM, Full width at Half Maximum

The calculated lattice values are a = 3.784742 Å and c =9.760094 Å , which are close to the standard lattice value of the tetragonal structure of TiO_2 a= 3.7842 Å and c = 9.5146 Å . The standard unit cell volume is 136.26 Å ^{3}, and from the values of a and c, the unit cell volume is 139.80624 Å ^{3} [25]. It confirms that Zn doping does not change the tetragonal structure of TiO_2.

The crystallite size S was estimated using Debye Scherrer as outlined by Kiprotich, S *et al.* 2018 [26] **Eq (3)**

$$S = W / \beta cos\theta \quad (3)$$

Where S is the average crystallite size of the NPs (nm), W is a constant (1.38645Å). W= **λ**×k where, when using CuKα radiation **λ**= 1.5406 Å and the Scherer's shape constant k= 0.9, β is the diffraction line broadening measured at half of its maximum intensity (rad) (FWHM), and θ is the Bragg's diffraction angle in rads.

As tabulated in **Table 1,** the average crystallite size for the doped compounds is found to decrease by 0.43 and 0.49 nm for the 1% and 10% Z-T NPs, respectively, and a slight increase of 0.25 nm for the 5% Z-T NPs with respect to the 0% Z-T NPs. The decrease from 13.75 nm to 9.32 nm for the

0% and 1% Z-T NPs is as a result of substitution doping. Zn atoms substitute Ti in Ti-O-Ti, forming Ti-O-Zn in the tetrahedral crystal lattice of TiO_2 with coordination number 6.

The substituted atoms of Ti occupy the interstitial position or other available sites in the crystal lattice to allow the crystal to adjust and maintain charge neutrality and structural stability. A similar ionic radius of 0.75 and 0.74 Å for Ti^{4+} and Zn^{2+} [14] enables Zn to form substitution doping at lower concentrations. Substitution doping by XRD analysis confirms FTIR analysis for the Zn-O stretching vibration at wave number 668 cm^{-1}. Lattice strain, attributed to the slight difference in ionic radius and different oxidation states, contributed to the reduced crystallite size. This strain distorts the lattice parameters by creating oxygen vacancies, filling interstitial sites, rearranging atoms, and reducing the charge to maintain crystal charge neutrality.

The values of strain were calculated using **Eq (4)** [27]

$$\varepsilon = \frac{\beta}{4tan\ \theta} \quad (4)$$

Where θ is the diffraction angle in rads, and β is the FWHM in rads.

The deviation of the lattice parameters were attributed to be due to defects caused by microstrain in the lattice [28]. The as-prepared Z-T NPs had a higher strain value than the un-doped T NPs. An increase in strain confirms the creation of defects in T NPs as the TiO_2 tries to accommodate the foreign atoms of Zn in its lattice structure. **Figure 3 (a)** confirms the inverse relationship between crystallite size and strain values. As tabulated in **Table 1,** strain values increase from 0.29208 to 0.66852 for 0% and 1% Z-T NPs, respectively. The strain values appear constant at 3, 5, and 7% Z-T NPs with a value of 0.48, a decrease of 0.18792. These values appear constant due to lattice strain relaxation brought by the increased presence of Zn atoms around the lattice structure of Ti-O-Zn. The relaxation allows the growth of crystallites from 9.32 to 13.95 nm for 1% and 5% Z-T NPs, respectively. The maximum substitution doping occurs at 5% Z-T NPs as it gives the highest crystallite size value for the Z-T NPs. The 7, 9, and 10% Z-T NPs form both substitution and interstitial doping as the extra Zn dopants atoms are forced to occupy the interstitial sites. Strain values increase from 0.48060 to 0.53594 for 5% and 10 % Z-T NPs, respectively.

Figure 3 (b) shows that the average crystallite size has an inverse proportional to FWHM with the highest value of 1.34392 at 1% Z-T NPs, twice the value at 0% Z-T NPs, as tabulated in **Table 1**. The increase in FWHM for the Z-T NPs is attributed to asymmetrical stretching from the Ti-O-Zn crystal disorder, leading to a broader peak. A higher specific surface area in photoanode is essential in maximizing light absorption, providing sufficient active sites for photochemical reactions, and promoting efficient charge separation and transport. The entire area that the crystals cover in unit mass was considered. The Surface Area (SSA) was calculated using **Eq (5)** [28] and tabulated in **Table 1**.

$$SSA = \frac{G}{S_p} \quad (5)$$

Where $G = \frac{6\times10^3}{\rho}\rho$ is the density of TiO_2 NPs (4.23g/cm^3) and S_p denoted the crystal size obtained by the Debye – Scherer equation

Figure 3 (c) confirms that SSA for TiO_2 NPs is inversely proportional to crystallite size. 10 % Z-T NPs had the highest value of 1.60367 M^2g^{-1} $\times10^{12}$ and a corresponding least crystallite value of 8.85 nm. 5 % Z-T NPs had the least SSA with 1.01645 M^2g^{-1} $\times10^{12}$ and a corresponding largest crystallite value of 13.95 nm.

To calculate dislocation density (δ) [29] **Eq (6)** was employed.

$$\delta = \frac{1}{S^2} \quad (6)$$

Where S is the crystallite size (nm) obtained from Debye-Scherer equation.

The calculated dislocation density values were tabulated in **Table 1** and presented in the plot compared to crystallite size, as shown in **Figure 3 (d)**. The dislocation network within the structure is indicated by the dislocation density and is inversely proportional to crystallite size; it was highest at 10% with 0.01278 and least at 5% Z-T NPs with 0.00514 line/ nm^3.

3.3. Optical Analyses

The optical properties of the various % Z-T NPs were analyzed using a UV-Vis 1800 Shimadzu model. **Figures 4 (a) and (b),** show reflectance spectra and the estimated band gap for the different mol % Z-T NPs.

Table 2. Estimated values of Reflectance edge, % Reflectance, and band gap energy for the different % Z-T NPs

% Z-T NPs	Reflectance edge (nm)	% Reflectance	Estimated Band gap energy (Eg), (eV)
0 % Z-T NPs	335.48	68.24	4.43
1 % Z-T NPs	316.52	39.16	5.00
2 % Z-T NPs	309.94	33.11	4.99
3 % Z-T NPs	326.51	33.57	5.14
5 % Z-T NPs	319.23	35.35	5.04
7 % Z-T NPs	306.72	34.37	4.98
9 % Z-T NPs	323.00	44.94	4.81
10 % Z-T NPs	310.72	45.02	4.92

Figure 4 (a) shows 2% Z-T NPs, with the lowest % reflectance of 33.11%, translating to the highest transmittance of 66.89%. The un-doped 0% Z-T NPs had the highest reflectance of 68.24%, as tabulated in **Table 2**. The band gap of a material defines its electronic condition.

The direct band gap of the Z-T NPs was approximated by using Tauc equation [30]. **Eq (7**)

$$(A\ hv)^{\gamma} = C(hv - Eg) \quad (7)$$

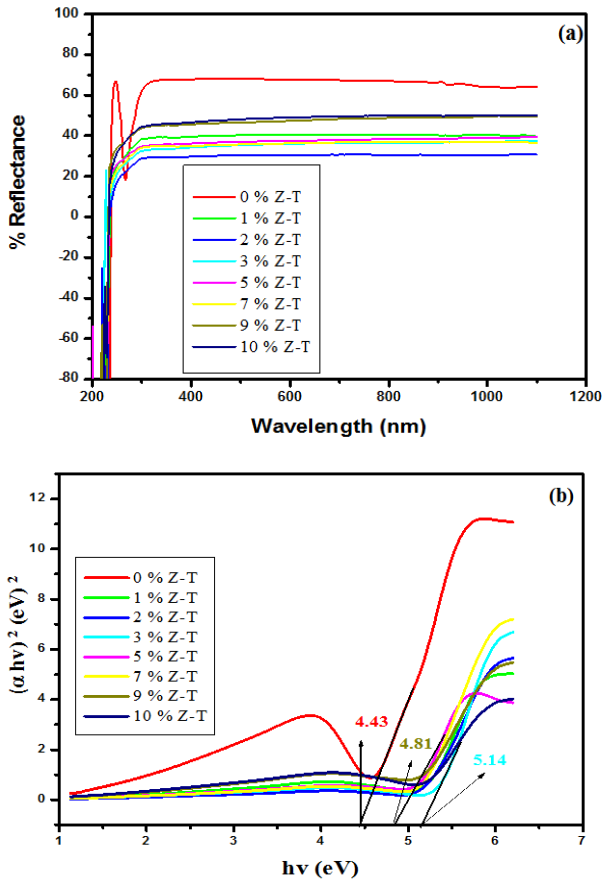

Figure 4. Plot displaying **(a)** Reflectance spectra and **(b)** Estimated band gap for different mol% Z-T NPs

For the direct band gap for the direct allowed transition, Tauc relation **Eq (8)** was used.

$$Ahv = C\sqrt{hv - Eg} \tag{8}$$

Where hv is the incident photon energy, C is the proportionality with a value of 1, Eg is the estimated electronic band gap and *A* is the absorption coefficient which can be determined using Beer-Lambert's formula and has a direct relationship to the measured absorbance. The intercept of the linear section of $(A\,hv)^2$ versus hv plot on the hv axis was used to determine the average energy band gaps as shown in **Figure 4 (b)**, [31,32].

Optical band gap values were estimated by drawing a tangent of $(\propto hv)^2$ Tauc's plot and extrapolating to the $(\propto hv)^2 = 0$ x axis, as shown in **Figure 4 (b).** The bulk band gap of T NPs for the anatase phase is 3.2 eV, the obtained values from the Tauc plot displayed greater optical values that are 4.43, 5.00, 4.99, 5.14, 5.04, 4.98, 4.81, and 4.92 for 0, 1, 2, 3, 5, 7, 9 and 10% Z-T NPs respectively. As tabulated in **Table 2,** the highest band gap was 3% Z-T NPs with an estimated value of 5.14eV, an increase of 0.69 from the 0% Z-T NPs. These discrepancies between the bulk and synthesized Z-T NPs occur due to quantum confinement effects where electrons are confined in three dimensions, leading to discrete energy levels, surface states, and defects attributed to high surface-to-volume ratio and size-dependent electronic properties where the energy levels of the conduction and valence bands shift influencing the overall band gap. Additionally, the decrease in the energy band gap observed can be attributed to the increase in the crystallite size of the Z-T NPs as reported by Kiprotich et al 2018 [33]. In their research, they reported a relationship where decrease in energy band gap was attributed to the enlargement of the NPs caused by the agglomeration of the particles.

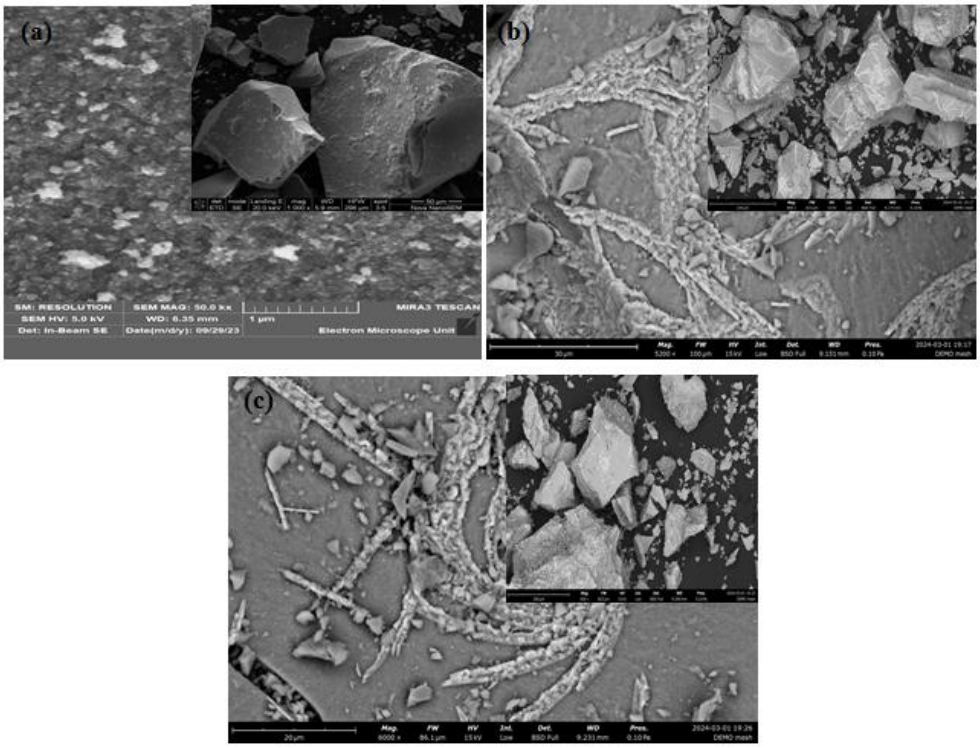

Figure 5. SEM representative images for **(a)** 0, **(b)** 5 and **(c)** 10 % Z-T NPs

Table 3 (a). Elemental compositions for 5 % Z-T NPs

	Element Number	Element Symbol	Element Name	Atomic Conc.	Weight Conc.
	8	O	Oxygen	61.356	31.000
	17	Cl	Chlorine	3.907	4.600
	22	Ti	Titanium	30.182	48.000
	30	Zn	Zinc	4.555	16.400

Table 3 (b). Elemental compositions for 10 % Z-T NPs

	Element Number	Element Symbol	Element Name	Atomic Conc.	Weight Conc.
	6	C	Carbon	1.400	0.600
	8	O	Oxygen	59.366	35.600
	17	Cl	Chlorine	2.450	3.100
	22	Ti	Titanium	29.024	49.600
	30	Zn	Zinc	7.759	11.100

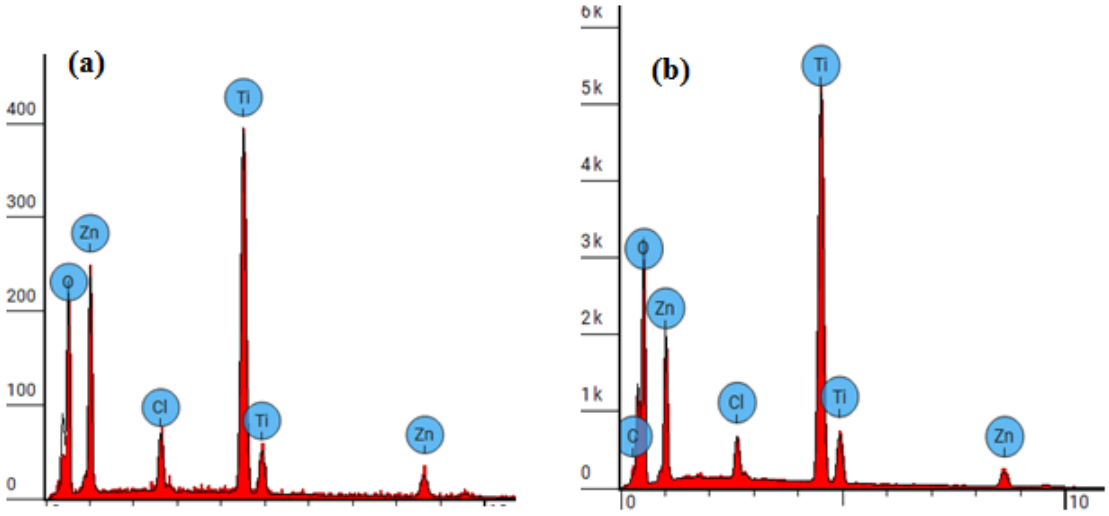

Figure 6. EDS spectra for **(a)** 5 % Z-T NPs and **(b)** 10 % Z-T NPs

3.4. Morphological Analysis

Figures 5(a), **(b),** and **(c)** depict the SEM morphology of 3 representative samples that are 0, 5, and 10% Z-T NPs, respectively. The 5 and 10% F-T NPs images show a dense particle compared to the 0% F-T NPs. The porosity and rough texture present at 0% Z-T NPs are due to nucleation on primary particles of TiO_2. The Z-T NPs samples are found to sinter; the surface deposits fuse to form a solid mass. The smooth surface and decreased porosity for 5 and 10% Z-T NPs lead to a more compact structure resulting from substitution and interstitial doping, as earlier confirmed by XRD and FTIR analysis. The increased particle size and formation of larger crystals for the doped samples result from increased agglomeration and aggregation, respectively, which further confirms doping helps improve the morphological properties of TiO_2. Similar results were obtained by Kiprotich et. Al 2016 where the agglomerations observed were due to Ostwald ripening process where smaller particles dissolve to form larger particles [34]. The coalescing of the particles to form a single unified entity for the Z-T NPs samples is in line with the improvement and increased crystallite size shown by XRD analysis.

Energy dispersive X-ray spectroscopy (EDS) analysis was carried out to determine the presence of elements in the Z-T NPs. **Figures 6 (a)** and **(b)** show the presence of Zn, Ti, and O and their atomic distribution, which agree with the expected composition. **Table 3 (a)** and **(b)** summarizes the atomic percentage of elements present in 5 and 10% Z-T NPs. The atomic percentage of Zn was higher at 10% compared to 5% Z-T NPs, in line with the different doping concentrations. During SEM analysis, the sample was held in place by a carbon stick, therefore the carbon atoms detected are from the carbon stick and the chloride present is from the stock solution of HCl used to adjust pH, which has not altered the properties of Z-T NPs. Therefore, the concentration of Zn^{2+} in T NPs can be controlled using different Zn^{2+} concentrations during the synthesis process.

4. Conclusions

In the present study, the sol-gel method was successfully used to synthesized Z-T NPs. FTIR showed stretching

vibration of Zn-O at wave number 668 cm^{-1}, confirming substitution doping at 1% Z-T NPs. As a result of substitution doping, XRD analysis showed crystallite size decreased due to the development of strain. Strain values were almost twice for the 1% doped compared to the 0% Z-T NPs. The strain value was constant between 3, 5, and 7% Z-T NPs due to the popularity of the Zn atom in the structure leading to strain relaxation. Zn doping is appropriate for smaller crystallite sizes with 10% Z-T NPs having 8.85 nm, a decline of 4.9 nm. The optical band gap was high compared to the bulk value of 3.2 eV. It was attributed to the quantum effect; however, the Z-T NPs had a higher band gap than the T NPs. UV- Vis 1800 Shimadzu model requires the analyte to be dissolved in a suitable solvent; Z-T NPs could not fully dissolve in absolute ethanol, leading to the reported discrepancies. EDS showed the inclusion of Zn atoms, confirming that Zn^{2+} ions were successfully doped in the TiO_2 crystal lattice. Therefore, the presence of Zn atoms in TiO_2 will enhance acceptor bands, improving its electron transfer properties.

ACKNOWLEDGEMENTS

This research was successful courtesy of the funding from DSA and Deep Learning Indaba through the African AI Research Grant.

Data Availability Statement

All data generated or analyzed during this study are included in the manuscript.

Conflict of Interest

The authors declare no conflict of interest.

REFERENCES

[1] Qureshi A A, Javed S, Javed HM, Akram A, Mustafa MS, Ali U, Nisar MZ. Facile formation of SnO2–TiO2 based photoanode and Fe3O4@ rGO based counter electrode for efficient dye-sensitized solar cells. Materials Science in Semiconductor Processing. 2021 Mar 1; 123: 105545.

[2] Sowmya S, Prakash P, Ruba N, Prabu AN, Janarthanan B, Reddy VR, Hegazy HH. Fabrication of natural dye-sensitized solar cells with bulk TiO2 instead of nano-sized. Optik. 2021 Sep 1; 242: 166205.

[3] Bashir S, Iqbal J, Farhana K, Jafer R, Hina M, Kasi R, Subramaniam RT. Hybrid organic polymer electrolytes for dye-sensitized solar cells. In Dye-Sensitized Solar Cells 2022 Jan 1 (pp. 181-212). Academic Press.

[4] Venkatraman MR, Rajesh G, Rajkumar S, Ananthan MR, Balaji G. Semi-transparent dye-sensitized solar cells (DSSC) for energy-efficient windows with microwave-prepared TiO2 nanoparticles as photoanodes. Materials Letters. 2024 Apr 1; 360: 135953.

[5] Mariotti N, Bonomo M, Fagiolari L, Barbero N, Gerbaldi C, Bella F, Barolo C. Recent advances in eco-friendly and cost-effective materials towards sustainable dye-sensitized solar cells. Green chemistry. 2020; 22(21): 7168-218.

[6] Zhu W, Wang S, Zhang X, Wang A, Wu C, Hao F. Ion migration in organic–inorganic hybrid perovskite solar cells: current understanding and perspectives. Small. 2022 Apr; 18(15): 2105783.

[7] Al-Ezzi AS, Ansari MN. Photovoltaic solar cells: a review. Applied System Innovation. 2022 Jul 8; 5(4): 67.

[8] Okil M, Salem MS, Abdolkader TM, Shaker A. From crystalline to low-cost silicon-based solar cells: A review. Silicon. 2022 Apr; 14(5): 1895-911.

[9] Devadiga D, Selvakumar M, Shetty P, Santosh MS. Recent progress in dye sensitized solar cell materials and photo-supercapacitors: A review. Journal of Power Sources. 2021 May 1; 493: 229698.

[10] Pallikkara A, Ramakrishnan K. Efficient charge collection of photoanodes and light absorption of photosensitizers: A review. International Journal of Energy Research. 2021 Feb; 45(2): 1425-48.

[11] Li Z, Li Z, Zuo C, Fang X. Application of nanostructured TiO2 in UV photodetectors: A review. Advanced Materials. 2022 Jul; 34(28): 2109083.

[12] Bashiri R, Mohamed NM, Sufian S, Kait CF. Improved photoelectrochemical hydrogen production over decorated titania with copper and nickel oxides by optimizing the photoanode and reaction characteristics. Materials Today Chemistry. 2020 Jun 1; 16:100241.

[13] Pastor E, Sachs M, Selim S, Durrant JR, Bakulin AA, Walsh A. Electronic defects in metal oxide photocatalysts. Nature Reviews Materials. 2022 Jul; 7(7): 503-21.

[14] de BemLuiz D, Andersen SL, Berger C, José HJ, Moreira RD. Photocatalytic reduction of nitrate ions in water over metal-modified TiO2. Journal of Photochemistry and Photobiology A: Chemistry. 2012 Oct 15; 246: 36-44.

[15] Wattanawikkam C, Pecharapa W. Synthesis and characterization of Zn-doped TiO2 nanoparticles via sonochemical method. Integrated Ferroelectrics. 2015 Sep 2; 165(1): 167-75.

[16] Jin EM, Jeong SM, Kang HC, Gu HB. Photovoltaic effect of metal-doped TiO2 nanoparticles for dye-sensitized solar cells. ECS Journal of Solid State Science and Technology. 2016 Feb 4; 5(5): Q109.

[17] Meesombad K, Sato N, Pitiphattharabun S, Panomsuwan G, Techapiesancharoenkij R, Surawathanawises K, Wongchoosuk C, Boonsalee S, Pee JH, Jongprateep O. Zn-doped TiO2 nanoparticles for glutamate sensors. Ceramics International. 2021 Aug 1; 47(15): 21099-107.

[18] Dubey RS, Jadkar SR, Bhorde AB. Synthesis and characterization of various doped TiO2 nanocrystals for dye-sensitized solar cells. ACS omega. 2021 Jan 29; 6(5): 3470-82.

[19] Rajaramanan T, Shanmugaratnam S, Gurunanthanan V, Yohi S, Velauthapillai D, Ravirajan P, Senthilnanthanan M. Cost

effective solvothermal method to synthesize Zn-Doped TiO2 nanomaterials for photovoltaic and photocatalytic degradation applications. Catalysts. 2021 May 29; 11(6): 690.

[20] Sharafi M, Oveisi H. A high-performance perovskite solar cell with a designed nanoarchitecture and modified mesoporoustitania electron transport layer by zinc nanoparticles impurity. Materials Science and Engineering: B. 2023 Oct 1; 296: 116608.

[21] Sa'aedi A, Akl AA, Hassanien AS. Effective role of Rb doping in controlling the crystallization, crystal imperfections, and microstructural and morphological features of ZnO-NPs synthesized by the sol–gel approach. CrystEngComm. 2022; 24(26): 4661-78.

[22] Khan SA, Khan SB, Khan LU, Farooq A, Akhtar K, AsiriAM. Fourier transform infrared spectroscopy: fundamentals and application in functional groups and nanomaterials characterization. Handbook of materials characterization. 2018: 317-44.

[23] Gakuru, S. W., Kiprotich, S., & Waithaka, P. (2024). Effects of growth temperature on the structural and optical properties of synthesized titanium dioxide nanoparticles. *American Journal of Materials Science*, *14*(1): 12-20.

[24] Nasiri S, Rabiei M, Palevicius A, Janusas G, Vilkauskas A, Nutalapati V, Monshi A. Modified Scherrer equation to calculate crystal size by XRD with high accuracy, examples Fe2O3, TiO2 and V2O5. Nano Trends. 2023 Sep 1; 3: 100015.

[25] Berger O. Understanding the fundamentals of TiO2 surfaces. Part I. The influence of defect states on the correlation between crystallographic structure, electronic structure and physical properties of single-crystal surfaces. Surface Engineering. 2022 Feb 1; 38(2): 91-149.

[26] Kiprotich S, Onani MO, Dejene FB. High luminescent L-cysteine capped CdTe quantum dots prepared at different reaction times. Physica B: Condensed Matter. 2018 Apr 15; 535: 202-10.

[27] Sutapa IW, Wahid Wahab A, Taba P, Nafie NL. Dislocation, crystallite size distribution and lattice strain of magnesium oxide nanoparticles. InJournal of Physics: Conference Series 2018 Mar 1 (Vol. 979, p. 012021). IOP Publishing.

[28] Muthee DK, Dejene BF. Effect of annealing temperature on structural, optical, and photocatalytic properties of titanium dioxide nanoparticles. Heliyon. 2021 Jun 1; 7(6).

[29] Velumani S, Mathew X, Sebastian PJ, Narayandass SK, Mangalaraj D. Structural and optical properties of hot wall deposited CdSe thin films. Solar energy materials and solar cells. 2003 Mar 31; 76(3): 347-58.

[30] Kiprotich S, Dejene BF, Onani MO. Effects of precursor pH on structural and optical properties of CdTe quantum dots by wet chemical route. Journal of Materials Science: Materials in Electronics. 2018 Sep; 29: 16101-10.

[31] Johannes AZ, Pingak RK, Bukit M. Tauc Plot Software: Calculating energy gap values of organic materials based on Ultraviolet-Visible absorbance spectrum. InIOP conference series: materials science and engineering 2020 Apr 1 (Vol. 823, No. 1, p. 012030). IOP Publishing.

[32] Haryński Ł, Olejnik A, Grochowska K, Siuzdak K. A facile method for Tauc exponent and corresponding electronic transitions determination in semiconductors directly from UV–Vis spectroscopy data. Optical Materials. 2022 May 1; 127: 112205.

[33] Kiprotich S, Dejene BF, Onani MO. Structural, optical and luminescence properties of CdTe quantum dots: Investigation on the effect of capping ligand ratio. Materials Research Express. 2018 Jun 13; 5(6): 065028.

[34] Kiprotich S, Dejene FB, Ungula J, Onani MO. The influence of reaction times on structural, optical and luminescence properties of cadmium telluride nanoparticles prepared by wet-chemical process. Physica B: Condensed Matter. 2016 Jan 1; 480: 125-30.